

Article

Strain-Induced Martensitic Transformation and Texture Evolution in Cold-Rolled Co–Cr Alloys

Yusuke Onuki ^{1,*} , Shigeo Sato ², Maiko Nakagawa ², Kenta Yamanaka ³ , Manami Mori ⁴, Akinori Hoshikawa ¹, Toru Ishigaki ¹ and Akihiko Chiba ³

¹ Frontier Research Center for Applied Atomic Sciences, Ibaraki University, 162-1 Shirakata, Tokai, Ibaraki 319-1106, Japan; akinori.hoshikawa.eml@vc.ibaraki.ac.jp (A.H.); toru.ishigaki.01@vc.ibaraki.ac.jp (T.I.)

² Graduate School of Science and Engineering, Ibaraki University, 4-12-1 Nakanarusawa, Hitachi, Ibaraki 316-8511, Japan; shigeo.sato.ar@vc.ibaraki.ac.jp (S.S.); 17nm537r@vc.ibaraki.ac.jp (M.N.)

³ Institute for Materials Research, Tohoku University, 2-1-1 Katahira, Aoba-ku, Sendai 980-8577, Japan; k_yamanaka@imr.tohoku.ac.jp (K.Y.); a.chiba@imr.tohoku.ac.jp (A.C.)

⁴ Department of Materials and Environmental Engineering, National Institute of Technology, Sendai College Natori, 48 Nodayama, Medeshima-Shiote, Natori 981-1239, Japan; m-mori@sendai-nct.ac.jp

* Correspondence: yusuke.onuki.0@vc.ibaraki.ac.jp; Tel.: +81-29-352-3234

Received: 31 March 2018; Accepted: 16 May 2018; Published: 22 May 2018



Abstract: Co–Cr alloys have been used in biomedical purposes such as stents and artificial hip joints. However, the difficulty of plastic deformation limits the application of the alloys. During the deformation, Co–Cr alloys often exhibit strain-induced martensitic transformation (SIMT), which is a possible reason for the low formability. The distinct increase in dislocation density in the matrix phase may also result in early fractures. Since these microstructural evolutions accompany the textural evolution, it is crucial to understand the relationship among the SIMT, the increase in dislocations, and the texture evolution. To characterize those at the same time, we conducted time-of-flight neutron diffraction experiments at iMATERIA beamline at the Japan Proton Accelerator Research Complex (J-PARC) Materials and Life Science Experimental Facility (MLF), Ibaraki, Japan. The cold-rolled sheets of Co–29Cr–6Mo (CCM) and Co–20Cr–15W–10Ni (CCWN) alloys were investigated in this study. As expected from the different stacking fault energies, the SIMT progressed more rapidly in the CCM alloy. The dislocation densities of the matrix phases of the CCM and CCWN alloys increased similarly with an increase in the rolling reduction. These results suggest that the difference in deformability between the CCM and CCWN alloys originate not from the strain hardening of the matrix phase but from the growth behaviors of the martensitic phase.

Keywords: Co–Cr alloy; strain-induced martensite transformation; neutron diffraction; iMATERIA; texture; phase fraction; dislocation density; CMWP method

1. Introduction

Co–Cr alloys have high strength, wear resistance, and biocompatibility, which are suitable for biomedical applications such as artificial joints [1]. In particular, the Co–Cr–Mo alloy is a representative Co–Cr-based alloy that has been used in this application. However, the formability of a Co–Cr–Mo alloy is not sufficient to apply various plastic forming, e.g., rolling, forging, and wire drawing. Therefore, an alloy with more plastic deformability, Co–Cr–W–Ni (known as L-605) has been applied to biomedical devices, e.g., vascular stents [2]. Although these alloys have expanded the applications of the biomaterials, further development is demanded to attract a wider application range and establish reliability.

In order to increase the performance of the Co–Cr alloy, plastic deformation mechanisms should be studied carefully. These alloys have quite low stacking fault energies (SFEs), which introduce strain-induced martensite transformation (SIMT) from face centered cubic (FCC) to hexagonal closest packed (HCP) martensite. Because dislocations in alloys with low SFE are dissociated into Shockley partial dislocations, cross slip of dislocations is inhibited and the dislocation glide is consequently restricted to the specific {111} plane. As a result, dislocation density can increase more rapidly with the increase in plastic strain. Furthermore, martensite can also be a barrier of dislocation glide, which is another suspicious source of strain hardening.

Therefore, we should focus on the development of dislocation structures and frequency of SIMT with increasing strain. It is also meaningful to observe the development of texture, which results from the slip deformation, i.e., activity of the dislocations.

The authors have recently developed a simultaneous measurement scheme for textures and phase fraction at iMATERIA, time-of-flight (TOF)-type neutron diffractometer at the Japan Proton Accelerator Research Complex (J-PARC) Materials and Life Science Experimental Facility (MLF), Ibaraki, Japan [3–6]. This measurement can also acquire a high-resolution diffractogram, which is suitable for line profile analysis to determine the dislocation density [6]. This paper reports the results of the above simultaneous measurements of three quantities, namely, texture, phase fraction, and dislocation density in rolled Co–Cr–Mo and Co–Cr–W–Ni alloys. On the basis of these results, the mechanisms of plastic deformation and strengthening are discussed.

2. Materials and Methods

The tested alloys were Co–29Cr–6Mo and Co–20Cr–15W–10Ni (mass %). They are respectively referred to as CCM and CCWN in the following text. The SFEs for CCM and CCWN are -100 mJ/m^2 and 60 mJ/m^2 , respectively, at room temperature [7]. The samples were initially prepared in the shape of $30 \text{ mm} \times 10 \text{ mm} \times 4 \text{ mm}$ in the rolling direction (RD), transverse direction (TD), and sample normal (ND), respectively. They were cold-rolled up to rolling reductions of 10%, 20%, 30%, and 40%. Rectangular specimens for the following neutron diffraction experiments were cut from the rolled samples. The dimensions of the specimen were 3 mm in the RD, 15 mm in the TD, and 4 mm in the ND. The specimens were inserted into the vanadium cells. The schematic for the sample setting geometry and the photograph of the vanadium cell are shown in Figure 1. Since the slit size of the incident beam was $20 \text{ mm} \times 20 \text{ mm}$, the sample volume was fully irradiated in the diffraction experiment.

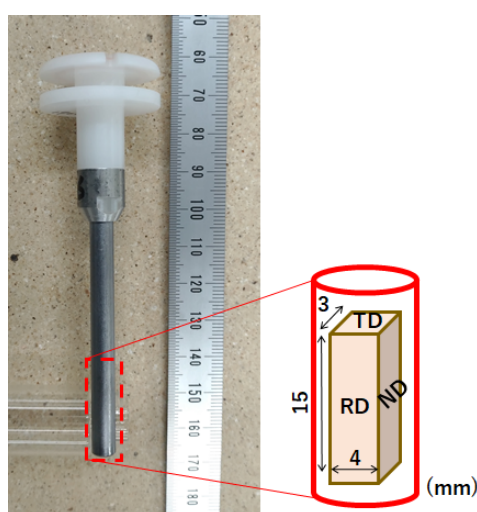


Figure 1. Vanadium cell used for the neutron diffraction experiments at iMATERIA, Japan Proton Accelerator Research Complex (J-PARC) Materials and Life Science Experimental Facility (MLF), Ibaraki, Japan. ND: sample normal; RD: rolling direction; TD: transverse direction.

The neutron diffraction measurement was conducted at iMATERIA, 20th beamline at J-PARC MLF [5]. The texture and phase fractions were analyzed by applying the Rietveld texture analysis (RTA) by using Materials Analysis Using Diffraction (MAUD) software [8]. The RTA is the compositional analysis of texture calculation and Rietveld method. In this analysis, the input data are 132 diffractograms measured by the observation points (OPs) locating at different positions. Since the diffraction pattern measured by each OP corresponds to a unique direction of the scattering vector, it is possible to observe the dependency of the diffraction intensities of all the peaks on the direction of the scattering vector. Based on the observed variation of diffraction intensities, the orientation distribution function (ODF) representing the texture of each phase is calculated by the extended Williams-Imhof-Matthies-Vinel (E-WIMV) method [8]. The result of the texture calculation is reflected on the diffractogram fitting, i.e., Rietveld analysis, as the preferential orientation correction factor. By repeating the ODF calculation and Rietveld pattern fitting, all the measured diffractograms are fairly fitted. Then it is possible to gain the most possible solutions of the ODF and Rietveld analysis including phase fraction. More details of the measurement at iMATERIA and subsequent RTA can be found in the previous papers by Onuki et al. [3,4]. It is often said that Co is not a suitable material for neutron diffraction due to its high absorption rate. However, we observed satisfactory diffractograms at all 132 detection points ($31^\circ \leq 2\theta \leq 161^\circ$). The absorption correction was applied with the harmonic coefficient model in MAUD, which considered the sample shape and the neutron beam paths.

The dislocation density was determined by using the convolutional multiple whole profile (CMWP) method [9,10] based on the diffractogram measured by the whole backscattering bank ($145^\circ < 2\theta < 165^\circ$) of iMATERIA. The dataset for the RTA and CMWP were constructed from the same event data, i.e., both could be obtained from the result of a single experiment.

Electron backscatter diffraction (EBSD) measurement was also conducted to confirm microstructural features by using the scanning electron microscope, JSM-6610LA (JEOL Ltd., Tokyo, Japan), equipped with EDAX OIM system. The measurement was conducted on the plane perpendicular to the TD. A map scanning was conducted on an area of $2.5 \text{ mm} \times 2.5 \text{ mm}$. The step size of 3–10 μm was applied depending on the microstructural features.

In order to clarify the plastic deformation mechanisms, numerical texture simulation was applied by using visco-plastic self-consistent model. The visco-plastic self-consistent (VPSC)-7 code written by Lebensohn and Tomé was used [11]. The tangent interaction model [11] was applied in this study. Although this software could not take SIMT into account, it was possible to obtain meaningful results by considering $\{111\}\langle 211\rangle$ twinning instead of the transformation. Both twinning and SIMT in low SFE FCC materials are resulted from the activation of $\{111\}\langle 211\rangle$ Shockley partial dislocations. Therefore, by finding twinned grains in the calculations, we can consider them as the transformed regions. To do this, we picked up the grains, which experienced large ($>15^\circ$) and discrete orientation changes, as the twinned grains. The PTR (predominant twin reorientation) scheme suggested by Tomé et al. [12] was applied to achieve the twin reorientation. In this scheme, grains with the twinning activation more than a threshold are fully reoriented. The applied deformation mode was plane strain compression deformation (i.e., $\varepsilon_x = -\varepsilon_z$, $\varepsilon_y = 0$) with a -0.03 increment of compressive strain. Four slip systems, (111) , $(\bar{1}\bar{1}1)$, $(\bar{1}\bar{1}\bar{1})$, and $(1\bar{1}\bar{1})$, were distinguished to apply larger ($1.4\times$) strain hardening among the different slip planes. This was applied based on the fact that planar accumulation of dislocations was often observed in low SFE alloys [13]. The same hardening rule was applied also for the twinning but the interaction between the 12 $\{111\}\langle 211\rangle$ twinning systems were not biased.

MTEX software was used for the smoothing, visualization, and introduction of the orthogonal sample symmetry for the discrete set of orientations [14].

3. Results

3.1. Texture

Figure 2 shows $\{111\}$ pole figures for the FCC phase in both CCM and CCWN alloys at various rolling reductions. Textures developed in both alloys with increasing rolling reduction, which indicates that the

FCC phases experienced the plastic deformation due to the dislocation slip. The main component of the texture locates between $\{011\}\langle 100\rangle$ (Goss) and $\{011\}\langle 2\bar{1}1\rangle$ (Brass) components for both alloys as shown in Figure 3. Copper component $\{112\}\langle 110\rangle$ can also be found as the minor component. These features are of a typical rolling texture for low SFE alloys at a moderate rolling reduction ($\sim 50\%$) [15].

The HCP martensite phases also indicate the developments of textures with increasing strain as shown in Figure 4. The maximum pole densities are found at positions $15\text{--}20^\circ$ away from the ND toward the RD.

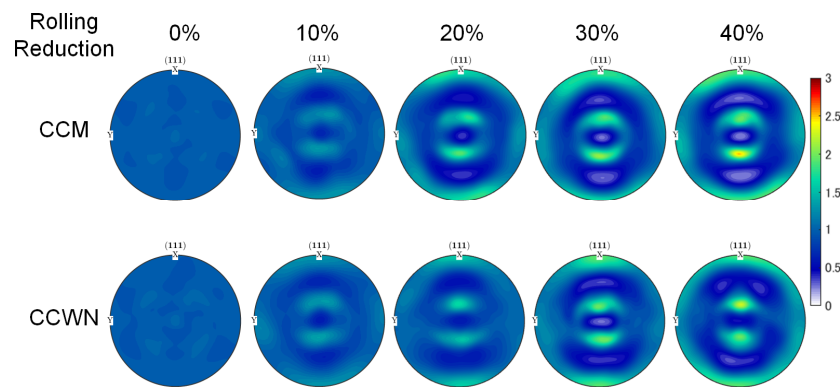


Figure 2. $\{111\}$ pole figures for face centered cubic (FCC) phases in the Co-29Cr-6Mo (CCM) and Co-20Cr-15W-10Ni (CCWN) alloys at various rolling reductions. The pole densities are expressed as multiples of the random density by color.

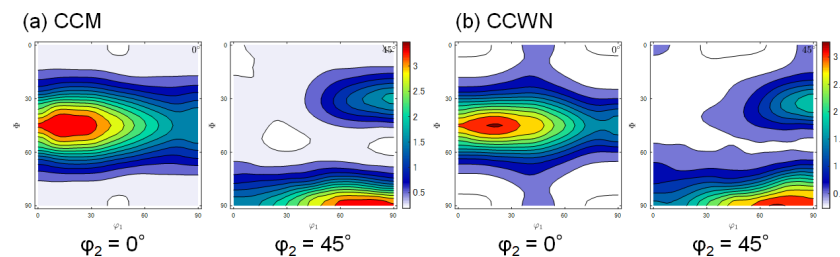


Figure 3. Orientation distribution functions (ODFs) for 40% rolled (a) CCM and (b) CCWN alloys. Contour lines are drawn with 0.25 increment of orientation densities.

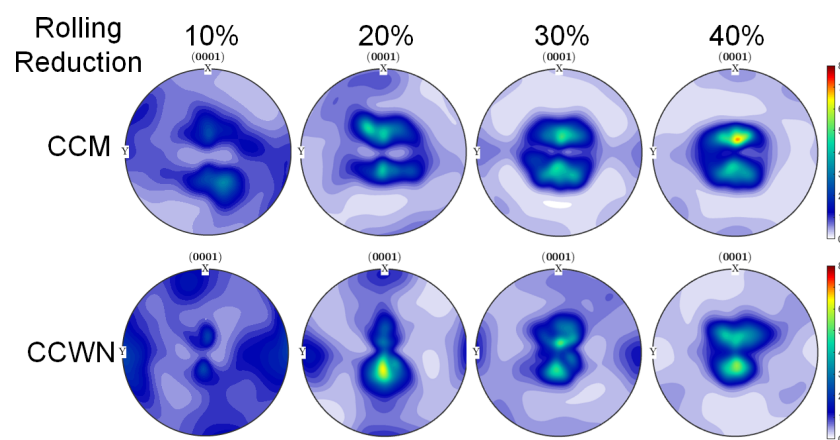


Figure 4. (0001) pole figures for hexagonal closest packed (HCP) martensite phases in the CCM and CCWN alloys at various rolling reductions. The pole densities are expressed as multiples of the random density by color.

3.2. Phase Fraction

Figure 5 shows the relationships between the volume fraction of the HCP martensite and rolling reduction for the CCM and CCWN alloys. In both alloys, the fractions of martensite monotonically increase with increasing rolling reduction. However, the CCM alloy shows an earlier increase of the martensite. In this figure, the results of EBSD measurement are also shown, which always indicate lower martensite fraction than the neutron diffraction measurement. This is probably because the EBSD measurement may skip small or thin second-phase particles. In the EBSD measurement, one should be careful with that the beam spot emitting the signal was only a few tens of nanometers in diameter, which is much smaller than the step size.

Figure 6 shows the results of the EBSD measurement and Back-scatter detector (BSE) image at higher magnification for the CCM alloy with 10% rolling reduction. As seen in Figure 6a, the grain structure of the FCC phases is well captured. In Figure 6b, some HCP particles are visible, whose areal fraction is 3.5%, as plotted in Figure 5. However, in the magnified BSE image (Figure 6c), thin plate-like structures can be found. According to Koizumi et al., these seem to be twin and/or HCP martensite [16]. It should be noted that this submicron structure is completely neglected in Figure 6a,b, i.e., EBSD measurement. As the above example indicates, small or thin particles tend to be neglected in the EBSD measurement. When the incident beam is shot on a boundary, an overlapping diffraction patterns from two orientations or phases are obtained, leading to a data point with no solution. Especially at higher strain, the diffraction patterns from near-boundary regions become unclear, resulting in failure of phase and orientation identification. These problems on and around the boundary also cause underestimation of the fraction of the finely distributed phase because the frequency of the boundary is higher for the finer particle. Although these problems can be minimized by optimizing the measurement conditions and surface preparation, one should always be careful with these issues. A similar problem has been pointed out in the case of the determination of meta-stable residual austenite fraction in bainitic/martensitic steels [17].

On the other hand, in the case of the RTA based on neutron diffraction, the input data are the diffractograms from the whole sample volume. Figure 7 shows the neutron diffractograms for the CCWN alloy measured by the whole BS ($145^\circ \leq 2\theta \leq 165^\circ$) bank of iMATERIA. At a rolling reduction of 20%, the diffraction peaks for the HCP martensite, for example 101_{HCP} , can be confirmed in Figure 6, while EBSD detected almost no martensite. In most cases, the shape and size of particles do not change the integrated diffraction intensity for the neutron diffractogram. Hence, we conclude that the results from the neutron-diffraction-based RTA are more reliable. The following discussion will be made on the basis of the results from the neutron diffraction.

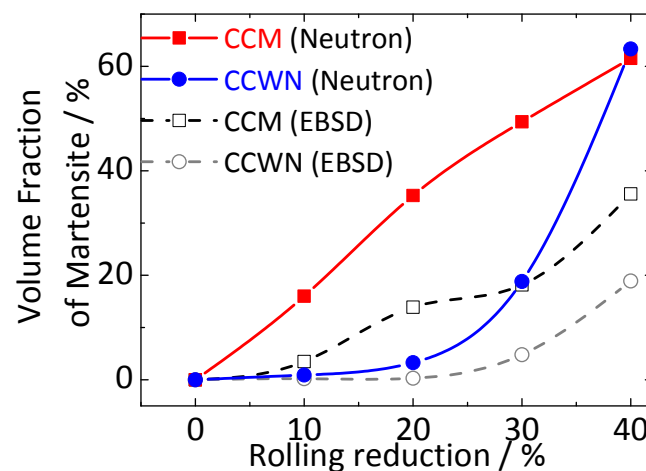


Figure 5. Relationships between the martensite phase fraction and the rolling reduction in the CCM and CCWN alloys. EBSD: Electron backscatter diffraction.

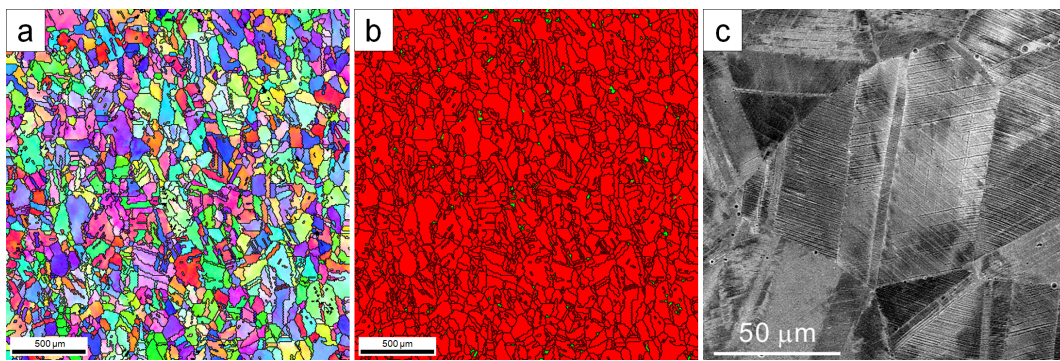


Figure 6. (a) Inverse-Pole-Figure map indicating crystal axes along the ND and (b) phase map (red: FCC, green: HCP) by EBSD, and (c) back-scattered electrons image of the CCM alloy rolled at 10%.

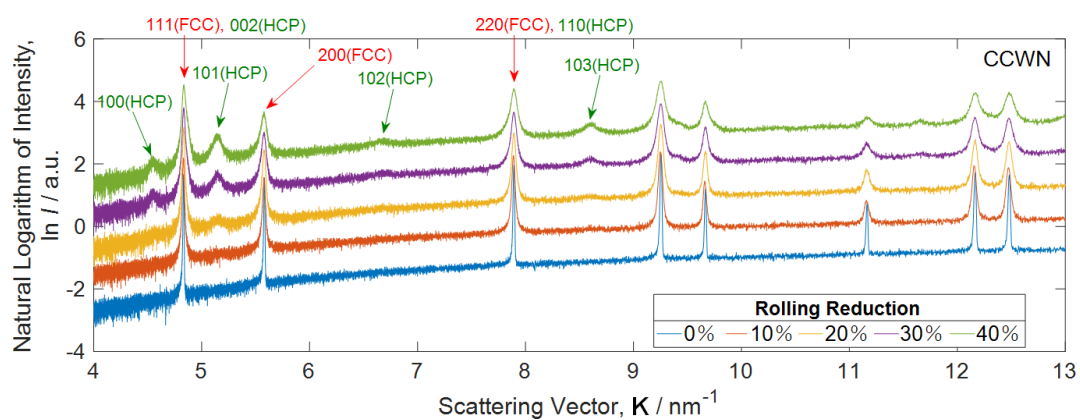


Figure 7. Neutron diffractograms measured by the backscattering bank of iMATERIA for the CCWN alloys at various rolling reductions ($K = 1/d = 2\sin\theta/\lambda$).

3.3. Characteristics of Dislocations and Crystallite

Dislocation density of the FCC matrix and HCP martensite phases were evaluated by the line-profile analysis. The CMWP [10] fitting to the neutron diffraction pattern of the CCM alloy rolled at 20% is shown in Figure 8 as an example of the line-profile analysis. Figure 9 shows the variations in dislocation density of both phases with the rolling reduction. While the dislocation densities of the FCC and HCP phases increased monotonically with an increase in the rolling reduction, the dislocation density of the HCP phase was higher than that of the FCC phase. Interestingly, the dislocation density of each phase for the CCM and CCWN alloys was almost comparable. The similarity of the texture evolution of the FCC phase of the CCM and CCWN alloys may originate from the similar degree of the contribution by dislocation slip as the plastic deformation mechanism.

Figure 10 shows the variations in area-weighted crystallite size with the rolling reduction. Generally, crystallite size is mainly affected by dislocation density [18]. The crystallite size of the HCP phase was almost comparable between the CCM and CCWN alloys in accordance with the similarity of their dislocation densities of both alloys. On the other hand, the crystallite size of the FCC phase of the CCM alloy was smaller than that of the CCWN up to the rolling reduction of 30%. The SIMT occurred at higher frequency in the CCM alloys as suggested from Figure 5, and grains of the FCC phase tends to be divided by the plate-like HCP phase as shown in Figure 6c. Consequently, the higher-frequency SIMT in the CCM alloy could further refine the crystallite. It should be noted that the crystallite size of the CCM alloy was comparable to that of the CCWN alloy at the rolling reduction of 40%, where the volume fraction of the martensitic phase of the CCWN alloy reached that of the CCM. This also suggests that the crystallite size is likely to be affected not only by dislocations but also martensite phase.

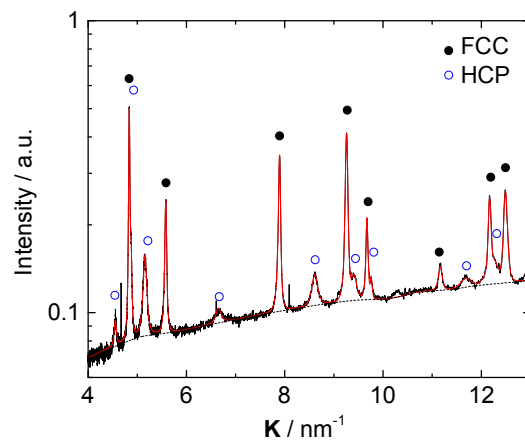


Figure 8. CMWP fitting to the neutron diffraction pattern of the CCM alloy rolled at 20%. ($K = 1/d = 2\sin\theta/\lambda$).

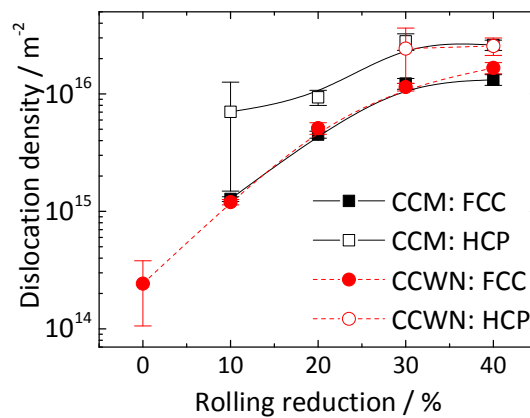


Figure 9. Variations in dislocation density of the FCC and HCP phases in the CCM and CCWN alloys.

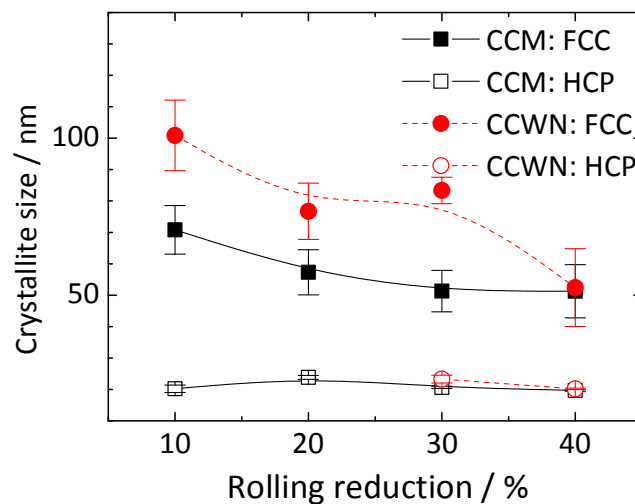


Figure 10. Variations in crystallite size of the FCC and HCP phases in the CCM and CCWN alloys.

4. Discussion

Based on the above results, one can find that the most notable difference between the CCM and CCWN alloys is the increasing rates of strain induced martensite phase. Since the CCM alloy has lower SFE, it may

have more chance to form the martensite phase. On the other hand, the increases of dislocation densities and texture developments in the FCC phases in both alloys are almost identical. Additionally, these results indicate that dislocation slip was quite active in the FCC phases. Therefore, it can be concluded that the better formability of the CCWN than that of CCM was due to the suppression of SIMT.

For this conclusion, however, we must show some evidence that the martensite acts as the hard obstacles introducing severe strain localization in the FCC phases. As shown in Figure 9, the HCP martensite tends to have high dislocation density, but the values are nearly constant irrespective to the rolling reduction. The main components of the textures of martensite phase also remain at the same positions. These facts indicate that the martensite phases merely experienced plastic deformation by dislocation slip.

Consideration using the numerical simulation also helps the above idea. In Figure 11, some results of the VPSC simulations are shown in $\varphi_2 = 0^\circ$ and 45° cross sections of ODFs. Figure 11a shows the result by considering only $\{111\}\langle 110 \rangle$ slip systems. The dominant component was Copper $\{211\}\langle 111 \rangle$, which is different from the experimental result (Figure 3). Figure 11b is the result considering both slip and twinning. The highest intensities locate at the Goss–Brass region, which agrees with Figure 3.

The Separation of not twinned and twinned grains (see Section 2) was conducted on this result and we obtained Figure 11c,d. It should be noted the grains consisting (c) was not reoriented by the twinning, the dominant component was not copper but brass. It can be understood by color that the ratio of copper to the Brass–Goss orientations in this result is quite similar to the experimental result. On the other hand, the twin-reoriented grains have orientation concentration around Goss orientation.

It is also possible to identify where the twinned grains came from in this simulation technique, as shown in Figure 11e. This figure indicates that the copper-oriented grains are preferentially consumed by the twinning. If we rephrase the word twinning to martensite transformation, it can be understood that Figure 11c corresponds to the residual FCC phase and the SIMT preferentially consumes the copper orientation.

As seen in Figure 4, the HCP martensite had high (0001) pole densities at the positions 15–20° away from the ND toward the RD. By considering the Shoji–Nishiyama orientation relationship [19], $(0001)_{\text{HCP}} \parallel (111)_{\text{FCC}}$, (111) should be oriented at those positions prior to the transformation. The Copper orientation has one of $\{111\}$ pole at positions 19.5° away from the ND toward the RD. Therefore, the texture of HCP martensite was formed by preferential transformation from the copper-oriented grains but NOT by the slip deformation.

As the conclusion, it is found that the main deformation mechanism is the dislocation slip in the FCC phase for both CCM and CCWN alloys. The strain-induced HCP martensite acts as the hard obstacle and divides the FCC matrix into small crystallites because of its plate-like morphology. Therefore, the occurrence of SIMT introduces strain hardening. The authors believe that the contribution of the SIMT as the shear deformation mechanism is quite limited. The SIMT from FCC to HCP is also reported in Fe–Mn–Si (–Cr) alloy, which is known as the shape memory alloy [20,21]. This alloy also shows very frequent SIMT with increasing strain. However, the recovery strain achieved by the transformation back from HCP to FCC is only a few percent. Although there are several reasons for the limited recovery for the Fe–Mn–Si alloy, it can be said that it is difficult to achieve a large strain only by the SIMT from FCC to HCP.

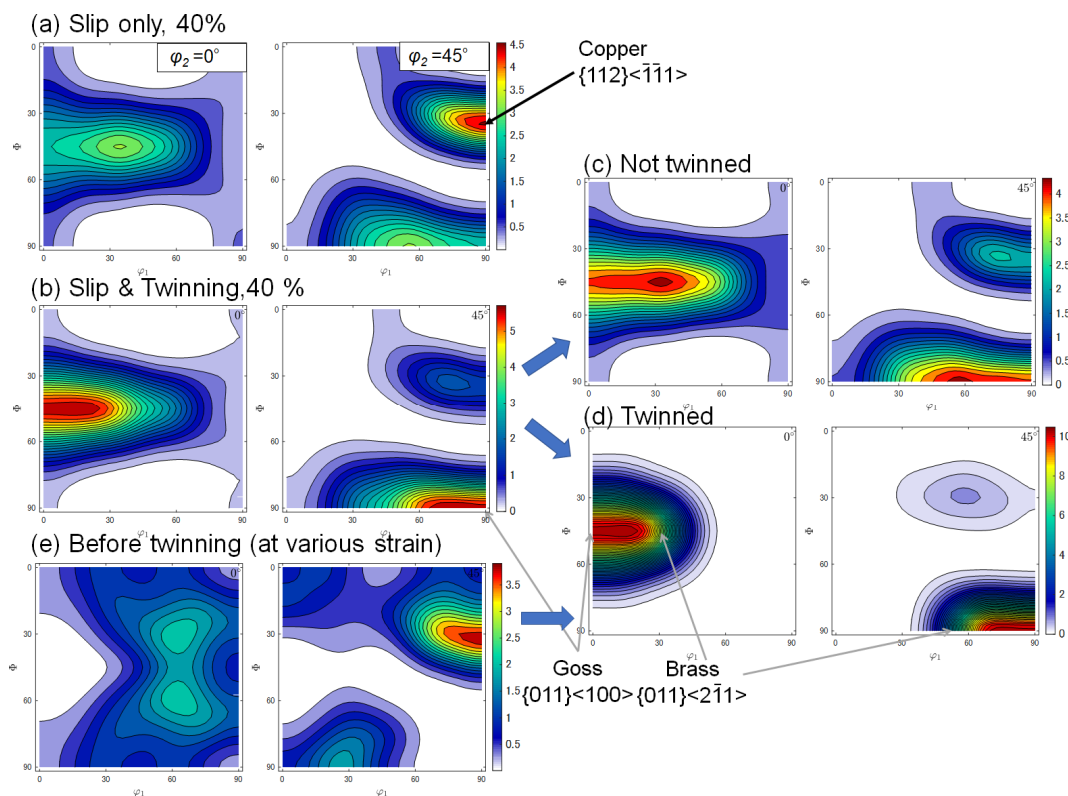


Figure 11. $\phi_2 = 0^\circ$ and 45° cross sections of ODFs generated by visco-plastic self-consistent (VPSC) simulation. 40% thickness reduction was introduced. (a) ODF formed by considering slip deformation only, (b) slip and twinning. Grains in (b) are separated between (c) which have not experienced the twin reorientation and (d) twinned grains. (e) Shows the parent orientations for the twinned grains shown in (d).

5. Conclusions

Time-of-flight neutron diffraction experiments were conducted in order to study the mechanisms of plastic deformation and work hardening in Co based alloys. The two types of alloys, CCM (Co–Cr–Mo) and CCW (Co–Cr–W), were examined at different degree of rolling. The following conclusions were obtained based on the Rietveld texture analysis and CMWP line profile analysis.

1. Both CCM and CCW alloys developed typical alloy-type textures at medium degree of rolling reduction, mainly consisted of the Brass and Goss components. The (0001) pole figures for the HCP martensite phases in both alloys had pole concentrations at $\pm 15\sim 20^\circ$ away from the ND toward the RD. The pole densities were increased with increasing strain while the positions of the maximum densities were almost unchanged.
2. The volume fraction of the strain-induced martensite increased with increasing rolling reduction in the CCM alloy. On the other hand, the CCW alloy showed only a few percent of martensite up to the rolling reduction of 20%. The martensite fraction rapidly increased after that and reached at the nearly same amount (~ 60 vol %) at the rolling reduction of 40%.
3. Dislocation densities in the FCC phases increased with increasing rolling reduction. The CCM and CCW alloys showed mostly the same values at any strain level. On one hand, the crystallite sizes in the CCM alloys were always smaller than in the CCW alloys. This is probably because the CCM alloy experienced more frequent grain subdivision by the formation of plate-shape martensite. The dislocation densities and crystallite sizes in the HCP phases were insensitive to the strain level in both alloys. Any distinct difference was not confirmed between the two alloys as for the HCP martensite.

4. The above analyses of texture and dislocation structure indicated that the plastic deformation of the tested alloys was achieved mainly by the dislocation slip in the FCC phase. The strain induced martensite phase seemed to behave as rigid particles, which merely experienced the dislocation slip. The VPSC texture calculation considering twin as the imaginary martensite was carried out to confirm this conclusion. The texture of the untwinned matrix grains well corresponded to the experimental FCC texture. The copper-oriented grains preferentially experienced twinning in the simulation, i.e., SIMT in reality. In fact, the peak positions on the measured (0001) pole figures corresponded to the positions of (111) pole of the copper orientation in FCC. Hence, we conclude that the observed textures of the martensite phases were resulted from the transformation with the Shoji–Nihshiyama relationship but not from the crystal rotation by the dislocation slip.

Author Contributions: Y.O., A.H., and T.I. optimized and conducted the neutron diffraction experiments; Y.O. also conducted the VPSC texture simulation and wrote some parts of the paper; S.S. designed and managed the overall research project and wrote the rest of the paper; M.N. conducted analyses and SEM/EBSD operation; K.Y., M.M., and A.C. prepared materials and supervised this work.

Funding: This work was financially supported by JSPS KAKENHI Grant Number 17H04957 and 16K21567.

Acknowledgments: The neutron diffraction experiments were conducted at iMATERIA (BL20) at J-PARC MLF as the project 2017PM0005. The authors appreciate Tetsuro Minemura and Toshiro Tomida, Ibaraki prefectural government for their kind support. This work was technically advised by the Research Society for quantum-beam analysis of microstructures and properties of steels.

Conflicts of Interest: The authors declare no conflict of interest.

References

1. Chiba, A.; Kumagai, K.; Nomura, N.; Miyakawa, S. Pin-on-disk wear behavior in a like-on-like configuration in a biological environment of high carbon cast and low carbon forged Co–29Cr–6Mo alloys. *Acta Mater.* **2007**, *55*, 1309–1318. [[CrossRef](#)]
2. Mani, G.; Feldman, M.D.; Patel, D.; Agrawal, C.M. Coronary Stents: A materials perspective. *Biomaterials* **2007**, *28*, 1689–1710. [[CrossRef](#)] [[PubMed](#)]
3. Onuki, Y.; Hoshikawa, A.; Sato, S.; Xu, P.G.; Ishigaki, T.; Saito, Y.; Todoroki, H.; Hayashi, M. Rapid measurement scheme for texture in cubic metallic materials using time-of-flight neutron diffraction at iMATERIA. *J. Appl. Cryst.* **2016**, *49*, 1579–1584. [[CrossRef](#)]
4. Onuki, Y.; Hoshikawa, A.; Sato, S.; Ishigaki, T.; Tomida, T. Rapid Measurement of Texture of Metals by Time-of-Flight Neutron Diffraction At iMATERIA And Its Applications. *J. Mater. Sci.* **2017**, *52*, 11643–11658. [[CrossRef](#)]
5. Ishigaki, T.; Hoshikawa, A.; Yonemura, M.; Morishima, T.; Kamiyama, T.; Oishi, R.; Aizawa, K.; Sakuma, T.; Tomota, Y.; Arai, M. IBARAKI materials design diffractometer (iMATERIA)—Versatile neutron diffractometer at J-PARC. *Nucl. Instrum. Methods Phys. Res. Sect. A* **2009**, *600*, 189–191. [[CrossRef](#)]
6. Nakajima, K.; Kawakita, Y.; Itoh, S.; Abe, J.; Aizawa, K.; Aoki, H.; Endo, H.; Masaki, F.; Kenichi, F.; Wu, G.; et al. Materials and Life Science Experimental Facility (MLF) at the Japan Proton Accelerator Research Complex II: Neutron Scattering Instruments. *Quantum Beam Sci.* **2017**, *1*, 9. [[CrossRef](#)]
7. Favre, J. Recrystallization of L-605 Cobalt Superalloy during Hot-Working Process. Ph.D. Thesis, INSA de Lyon, Villeurbanne, France, 2012.
8. Lutterotti, L.; Matthies, S.; Wenk, H.-R.; Schultz, A.J.; Richardson, J.W. Combined texture and structure analysis of deformed limestone from time-of-flight neutron diffraction spectra. *J. Appl. Phys.* **1997**, *81*, 594–600. [[CrossRef](#)]
9. Ribárik, G.; Gubicza, J.; Ungár, T. Correlation between strength and microstructure of ball-milled Al–Mg alloys determined by X-ray diffraction. *Mater. Sci. Eng. A* **2004**, *387*, 343–347. [[CrossRef](#)]
10. Hanawa, K.; Onuki, Y.; Todoroki, H.; Saito, Y.; Suzuki, S.; Sato, S. Effect of Scattering Vector of Neutron Diffraction for Rolled Steel Sheets on Neutron Diffraction Line-Profile Analysis. *Adv. X-ray Chem. Anal. Jpn.* **2017**, *48*, 338–345.
11. Lebensohn, R.A.; Tomé, C.N. A self-consistent anisotropic approach for the simulation of plastic deformation and texture development of polycrystals: Application to zirconium alloys. *Acta Metall. Mater.* **1993**, *41*, 2611–2624. [[CrossRef](#)]

12. Tomé, C.N.; Lebensohn, R.A.; Kocks, U.F. A model for texture development dominated by deformation twinning: Application to zirconium alloys. *Acta Metall. Mater.* **1991**, *39*, 2667–2680. [[CrossRef](#)]
13. Leffers, T.; Ray, R.K. The brass-type texture and its deviation from the copper-type texture. *Prog. Mater. Sci.* **2009**, *54*, 351–396. [[CrossRef](#)]
14. Bachmann, F.; Hielscher, R.; Schaeben, H. Texture Analysis with MTEX—Free and Open Source Software Toolbox. *Solid State Phenom.* **2010**, *160*, 63–68. [[CrossRef](#)]
15. Dillamore, I.L.; Roberts, W.T. Preferred orientation in wrought and annealed metals. *Metall. Rev.* **1965**, *10*, 271–380.
16. Koizumi, Y.; Suzuki, S.; Yamanaka, K.; Lee, B.-S.; Sato, K.; Li, Y.; Kurosu, S.; Matsumoto, H.; Chiba, A. Strain-induced martensitic transformation near twin boundaries in a biomedical Co–Cr–Mo alloy with negative stacking fault energy. *Acta Mater.* **2013**, *61*, 1648–1661. [[CrossRef](#)]
17. Jacques, P.J.; Allain, S.; Bouaziz, O.; De, A.; Gourgues, A.F.; Hance, B.M.; Houbaert, Y.; Huang, J.; Iza-Mendia, A.; Kruger, S.E.; et al. On measurement of retained austenite in multiphase TRIP steels—Results of blind round robin test involving six different techniques. *Mater. Sci. Technol.* **2009**, *25*, 567–574. [[CrossRef](#)]
18. Sato, S.; Kuroda, A.; Satoh, K.; Kumagai, M.; Harjo, S.; Tomota, Y.; Siato, Y.; Todoroki, H.; Onuki, Y.; Suzuki, S. In-situ observation of dislocation evolution in ferritic and austenitic stainless steels under tensile deformation by using neutron diffraction. *Tetsu-to-Hagané* **2018**, *104*, 201–207. [[CrossRef](#)]
19. Nishiyama, Z. *Martensitic Transformation*; Academic Press: New York, NY, USA, 1978; pp. 48–52.
20. Sato, A.; Chishima, E.; Yamaji, Y.; Mori, T. Orientation and composition dependencies of shape memory effect IN Fe–Mn–Si alloys. *Acta Metall.* **1984**, *32*, 539–547. [[CrossRef](#)]
21. Kwon, E.P.; Fujieda, S.; Shinoda, K.; Suzuki, S. Texture evolution and fcc/hcp transformation in Fe–Mn–Si–Cr alloys by tensile deformation. *Mater. Sci. Eng. A* **2010**, *527*, 6524–6532. [[CrossRef](#)]



© 2018 by the authors. Licensee MDPI, Basel, Switzerland. This article is an open access article distributed under the terms and conditions of the Creative Commons Attribution (CC BY) license (<http://creativecommons.org/licenses/by/4.0/>).